Optics Letters

Irradiance enhancement and increased laser damage threshold in As_2S_3 moth-eye antireflective structures

R. Joseph Weiblen,[1,*] Catalin M. Florea,[2,4] Lynda E. Busse,[3] L. Brandon Shaw,[3] Curtis R. Menyuk,[1] Ishwar D. Aggarwal,[2] and Jasbinder S. Sanghera[3]

[1]University of Maryland Baltimore County, Baltimore, Maryland 21250, USA
[2]Sotera Defense Solutions, Annapolis Junction, Maryland 20701, USA
[3]Naval Research Laboratory, Code 5620, Washington, DC 20375, USA
[4]Current address: Avo Photonics, Horsham, Pennsylvania 19044, USA
*Corresponding author: ro2@umbc.edu

Received 14 July 2015; revised 3 September 2015; accepted 9 September 2015; posted 10 September 2015 (Doc. ID 245960); published 15 October 2015

It has been experimentally observed that moth-eye antireflective microstructures at the end of As_2S_3 fibers have an increased laser damage threshold relative to thin-film antireflective coatings. In this work, we computationally study the irradiance enhancement in As_2S_3 moth-eye antireflective microstructures in order to explain the increased damage threshold. We show that the irradiance enhancement occurs mostly on the air side of the interfaces and is minimal in the As_2S_3 material. We give a physical explanation for this behavior.

OCIS codes: (310.6628) Subwavelength structures, nanostructures; (350.1820) Damage.

http://dx.doi.org/10.1364/OL.40.004799

It has been known since the time of Lord Rayleigh that microscale structures on the surface of optical interfaces are effective at reducing Fresnel reflections [1]. Periodic antireflective (AR) microstructures are called "moth-eye" structures because of their similarity to the microstructures on the eyes of nocturnal moths [2]. Moth-eye structures are a microstructured AR surface structure that are effective at reducing Fresnel reflections [3]. In the long wavelength limit, they work by providing a gradual change of the effective refractive index as light propagates across the air–glass interface. They are especially useful for high-index materials, which includes most mid-IR materials, such as chalcogenide glasses. Reducing Fresnel reflections from optical interfaces is important in mid-IR applications where high power and low loss are needed. High-power laser radiation that reflects from interfaces can damage instruments, while insertion or coupling losses can be major contributors to overall losses in a system [4]. Hence, mid-IR systems can greatly benefit by using moth-eye structures to reduce reflections from and increase transmission through interfaces. They are useful in a number of applications, including laser systems [4], photovoltaics [5], LEDs [6], automotive glass [7], electronics displays [8], and fiber optics [9].

Sanghera *et al.* [9] and MacLeod *et al.* [10] recently demonstrated a direct stamping method for imprinting these moth-eye structures on the end faces of chalcogenide optical fibers, where AR interfaces are particularly useful because of the large refractive index difference between air and As_2S_3 (~2.45 at a wavelength of $\lambda = 2$ μm). The direct stamping method allows structures to be accurately replicated, and the reflection as a function of wavelength depends sensitively on the structures and their parameters [11], which means that they must be accurately modeled. Because, in this case, the microstructure feature dimensions are on the same order as the wavelength of the incoming radiation (~1 μm), light in adjacent features interacts, and thus neither the long-wavelength average refractive index model nor the short-wavelength ray optics model is appropriate to describe transmission through moth-eye structures. Hence, they must be modeled using rigorous computational methods [12], such as the finite-difference time-domain method (FDTD) [13,14] or rigorous coupled-wave analysis (RCWA) [15,16], where the results become exact in principle as the grid size and step size tend to zero (FDTD) or the number of harmonics becomes infinite (RCWA).

Moth-eye structures have several advantages over traditional thin-film AR coatings, including environmental tolerance, surface adhesion, single material fabrication, minimal surface preparation, and self-cleaning via the lotus effect [7,9]. Additionally, in recent years it has been shown that in many cases periodic moth-eye structures have a higher laser-induced damage threshold (LIDT) than do traditional AR-coated surfaces [17–19]. In fact, the highest LIDT in fused quartz to date was recently demonstrated using moth-eye structures [20]. While both traditional AR coatings and moth-eye-structured surfaces usually have LIDTs lower than bulk material, damage in traditional AR coatings can occur at low laser fluences due to surface imperfections, thermal coefficient mismatch, and poor

layer adhesion. In moth-eye-structured surfaces, however, higher laser fluences cause localized melting of the surface structures before catastrophic damage occurs, often allowing the optics to continue performing albeit with reduced transmission, which can be very important in some applications.

The increased LIDT in moth-eye structures may seem counterintuitive, since it might be expected that the microstructured surface causes field enhancement. This field enhancement should reduce the amount of energy per unit area required to cause catastrophic damage. In this work, we show results for three particular moth-eye structures and calculate the time-averaged Poynting flux density in and around the microstructured surface to investigate why moth-eye structures are resistant to laser damage. Similar results with two other structure shapes indicate that these results hold generally for any appropriately designed moth-eye structure, regardless of feature shape or dimensions. We previously showed that, indeed, localized field enhancement does occur, but mostly on the air side of the air–glass interface [21]. Here, we additionally show results for a different feature shape, and we give a physical explanation for this behavior. We show that this behavior can be understood physically as a consequence of the oblique incidence of the waves on the walls of the moth-eye structure and the standard boundary conditions for electromagnetic waves at an interface.

In previous work [11], we studied theoretically the transmissivity of moth-eye structures on the end faces of As_2S_3 chalcogenide optical fibers using the FDTD method. Our computer model was able to reproduce the experimentally recorded transmissivity. We found that indeed the transmissivity is highly dependent on the exact shape and dimensions of the surface element features, which necessitates the use of a rigorous computational method. We showed that moth-eye structure surfaces can be designed to theoretically give near-perfect (greater than 99%) transmission for wavelengths from 2–5 μm.

Much theoretical work has investigated damage mechanisms in traditional thin-film coatings, particularly "nodule" defects, cf. [22,23]. The exact mechanisms for damage in particular thin-film coatings may be unknown, and possibilities, including avalanche ionization, dielectric breakdown, or thermal effects, can vary depending on the pulse duration, pulse repetition rate, spot size, and peak power of the laser input [24].

Jing *et al.* [25] studied localized enhancement in two-dimensional (2D) moth-eye structures with a triangular cross section in the visible spectral region. They showed that the field enhancement is highly dependent on the aspect ratio of the microstructure for the TE polarization, but does not vary significantly for the TM polarization. It can be shown, for a circularly symmetric three-dimensional microstructure in a square or hexagonal packing scheme, such as the structures we study here, that there should be no dependence on polarization as long as the incident light is normal to the surface [26,27]. Therefore, in our work, it is sufficient to study a single polarization.

In our computer model, we study moth-eye surfaces that are either "positive," i.e., raised from the surface, or "negative," i.e., depressed into the surface. We calculate the time-averaged Poynting flux for both positive and negative structure surfaces using RCWA with diffraction orders up to ±9 included in the calculation. We have verified that increasing the number of harmonics does not influence the results.

The Poynting flux is given by $\mathbf{S} = \mathbf{E} \times \mathbf{H}$. Its time average over one period is given by $\langle \mathbf{S} \rangle = (1/T) \int_0^T \mathbf{S}(t) \mathrm{d}t$. The time-averaged Poynting flux, also called irradiance, measured in Wm^{-2}, represents the rate of energy transfer per unit area. Areas that experience a higher energy flux density (a higher Poynting flux) should experience damage first.

We first consider a moth-eye structure with the shape of a truncated cone, which has a base width of 400 nm, a height of 800 nm, and a tip width of 200 nm. The features are square-packed with a period of 920 nm. Figure 1 shows the shape of the moth-eye structure models used for this study. The region of our computation includes the incident medium, air, on top of the As_2S_3 microstructure, which sits on an infinitely thick substrate of As_2S_3. The features shown here represent a single unit cell in an infinite 2D array. The positive shape is similar to the structure used to validate our model in [11]. The positive and negative shapes are mirror images; the negative shape is the feature that would be created if the positive shape were stamped into the As_2S_3 glass and vice versa.

Figure 2 shows the total transmission spectrum, including all diffracted orders, of the positive truncated cone features for light incident on the microstructured surface from the air above it. The transmission increases rapidly as the wavelength decreases below 1.8 μm because higher diffracted orders increase in number and intensity as the wavelength decreases. While it is true that diffraction orders greater than zero are predicted to exist for wavelengths below 2.25 μm, we have verified that higher diffracted orders do not carry energy at $\lambda = 2$ μm, the wavelength used for these studies. While other structures have better antireflective performance [11,28], this structure remains partially antireflective above 2 μm since the transmission of a plane surface is 0.83.

The input field is a CW plane wave with a wavelength of $\lambda = 2$ μm, normally incident on the structure in a *p*-polarization, so that the electric field is oriented in the *x*-direction. We take the refractive index of As_2S_3 to be $n = 2.45$ at 2 μm. We do not consider absorption in this work, i.e., $\mathrm{Im}(n) = 0$. As_2S_3 has a linear loss at 2 μm of about 0.5 dB/m, which means that

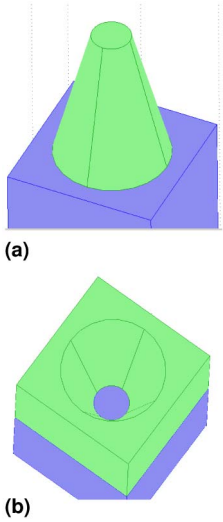

Fig. 1. Comparison of positive and negative moth-eye structures used in the computer simulation. Green areas show the As_2S_3 microstructure, and blue areas show the underlying As_2S_3 glass substrate. (a) Positive truncated cone. (b) Negative truncated cone.

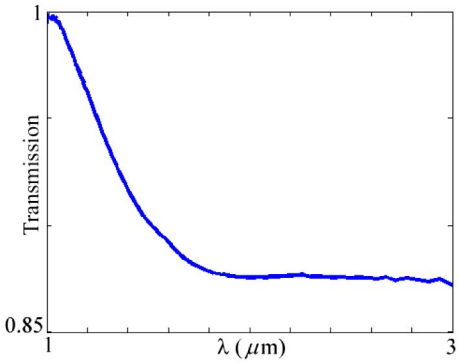

Fig. 2. Transmission spectrum of the truncated cone moth-eye structure.

a wave traveling through the tallest part of the microstructure considered here would lose a fraction 10^{-7} of its power to absorption over the region considered in this work. Thus, an input with a power of 1 kW would cause absorption of less than 0.1 mW over the region of these calculations.

Figure 3 shows the time-averaged Poynting flux $\langle \mathbf{S} \rangle$ (irradiance) in the microstructure as a function of position for the two structures. The figures show a slice through the unit cell, with the black lines delineating the microstructure. In all plots, the incoming field propagates downward from the top of the figure—for the negative structures, near the base of the cone, and for positive structures, near the tip of the cone. Figures 3(a) and 3(b) show the case of the positive cone feature, while Figs. 3(c) and 3(d) show the case of the negative cone feature. Figures 3(a) and 3(c) are in the plane of the incoming electric field, while Figs. 3(b) and 3(d) are oriented along a plane that is orthogonal to the plane of the incoming electric field.

For a positive cone, Figs. 3(a) and 3(b) show a large enhancement of the irradiance around the outer sides of the cone, with greatly decreased irradiance around the inner sides. For a negative cone, Figs. 3(c) and 3(d) show the greatest enhancement around the inner sides of the cone, with cool spots outside the depression and inside the As_2S_3 glass. The narrow end of the cone, the deepest part of the negative feature, shows the highest concentration of field energy, whereas, for a positive structure, the opposite is the case. Since the materials in the positive and negative case are inverted, we find in both cases that the air sides of the lateral cone surface have the greatest Poynting flux, while the glass sides of the lateral cone surface have the lowest Poynting flux. Additionally, there is a small area of slightly increased Poynting flux near the center of the glass part of the microstructure, corresponding to the center of the base of the cone in the positive structure.

We find that the positive truncated cone structure shows greater localization of the enhancement compared to the negative structure. The slices out of the plane of the incoming electric field also show greater localization of enhancement.

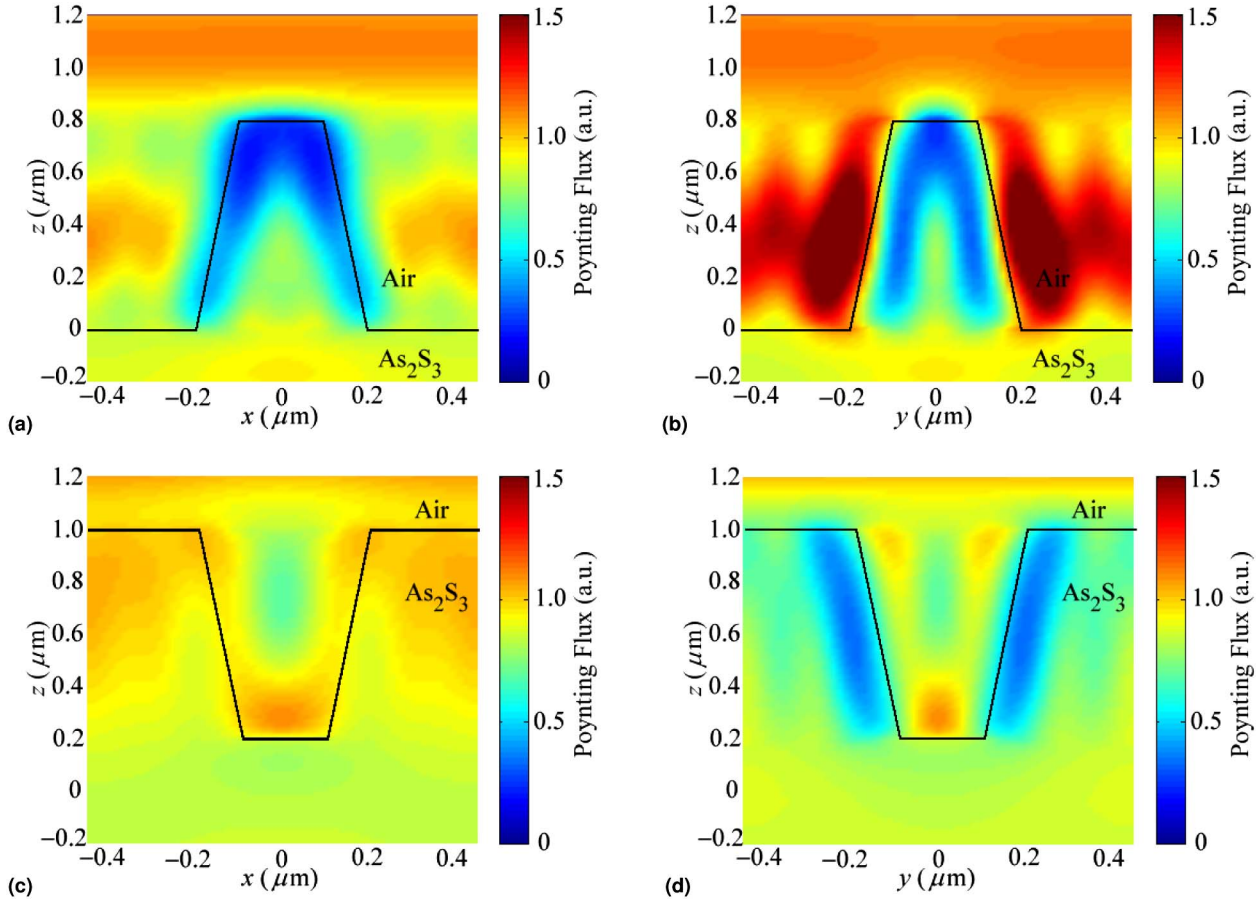

Fig. 3. Average Poynting flux density in truncated cone structures with *p*-polarized incident light (electric field oriented along the *x*-direction). (a) Positive cone at $y = 0$ (*x*-slice). (b) Positive cone at $x = 0$ (*y*-slice). (c) Negative cone at $y = 0$ (*x*-slice). (d) Negative cone at $x = 0$ (*y*-slice).

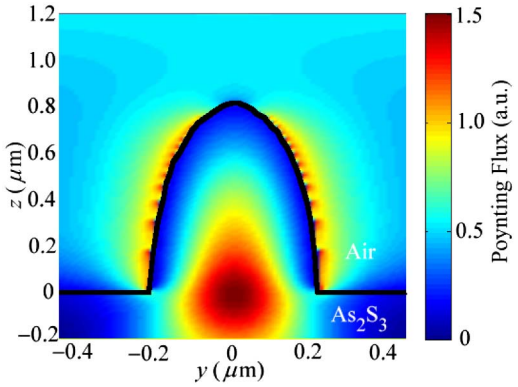

Fig. 4. Average Poynting flux density in a half-ellipsoidal structure at $x = 0$ (y-slice).

We may physically understand the decreased irradiance inside the glass by first noting that the propagation is highly oblique with respect to the sides of the microstructures, i.e., the angle of incidence with respect to the normals is nearly 90°. We next recall that the normal displacement field $\mathbf{D}$ will be continuous across an interface, so that the electric field $\mathbf{E} = \mathbf{D}/\epsilon$ is reduced in the higher-index material. Since the irradiance or Poynting flux $\mathbf{S}$ is proportional to the electric field according to $\mathbf{S} = \mathbf{E} \times \mathbf{H}$, it will be reduced in the lower index material in the plane of the electric field, regardless of whether the microstructures are positive or negative. Conversely, the irradiance will be enhanced out of the plane of the electric field since the total irradiance is fixed. This principle is used to guide radiation in the low-index region of slot waveguides [29]. These results are consistent with experimental results, which show catastrophic damage at higher laser fluences; the glass part of the microstructure is subjected to less irradiance as a result of the field enhancement.

To verify the intuition that similar results will hold for other moth-eye structures with different feature shapes and dimensions, we calculated the time-averaged Poynting flux $\langle \mathbf{S} \rangle$ in a positive half-ellipsoidal element with the same base width, height, and feature spacing, using the same input source and model setup. The results, shown in Fig. 4, are similar to those for the truncated cone: the areas of highest irradiance are on the air side of the air–glass interface on the lateral sides of the microstructure. We have seen similar results with pyramids and sinusoidally shaped elements. Hence it is reasonable to conclude that any properly designed moth-eye structure will exhibit similar behavior.

For an ideal thin-film AR coating, there will be no reflection at the design wavelength, and all of the flux density will be equal through the air above the coating, each layer of the coating, and the substrate below. In an ideal case, there will be no enhancement of the irradiance, which also means no decrease in irradiance in the coating, as is seen in moth-eye structures. However, in the case of a defect in the coating, there will be enhancement around that defect [23].

In conclusion, we have studied the time-averaged Poynting flux in moth-eye structures in As_2S_3 glass. We showed that the field enhancement from the microstructure is mostly in the air, rather than the glass, which explains the experimentally observed increase in the laser damage threshold. We found qualitatively similar results for both positive and negative moth-eye structures. However, positive structures showed greater enhancement localization. Enhancement was also greater out of the plane of the input electric field. We explained these results using Maxwell's equations and the associated boundary conditions.

This work may have practical applications beyond explaining the increase in laser damage threshold. For example, surface-enhanced Raman scattering (SERS) is due to the field enhancement facilitated by the microstructuring of the surface. Using this method, SERS structures could be designed to increase the enhancement and optimize its location.

Funding. Naval Research Laboratory (N00173-09-2-C016, N00173-15-1-G905).

REFERENCES

1. L. Rayleigh, Proc. London Math. Soc. **S1-11**, 51 (1879).
2. C. G. Bernhard and W. H. Miller, Acta Physiol. Scand. **56**, 385 (1962).
3. S. Chattopadhyay, Y. F. Huang, Y. J. Jen, A. Ganguly, K. H. Chen, and L. C. Chen, Mater. Sci. Eng. **69**, 1 (2010).
4. J. Kulakofsky, W. Lewis, M. Robertson, T. Moore, and G. Krishnan, Proc. SPIE **4679**, 198 (2002).
5. S. A. Boden and D. M. Bagnall, Prog. Photovoltaics **18**, 195 (2010).
6. Y. Ou, D. Corell, C. Dam-Hansen, P. Petersen, and H. Ou, Opt. Express **19**, A166 (2011).
7. D. S. Hobbs, B. D. MacLeod, and J. R. Riccobono, Proc. SPIE **6545**, 65450Y (2007).
8. T. Hoshino, M. Itoh, and T. Yatagai, Appl. Opt. **46**, 648 (2007).
9. J. Sanghera, C. Florea, L. Busse, B. Shaw, F. Miklos, and I. Aggarwal, Opt. Express **18**, 26760 (2010).
10. B. D. MacLeod, D. S. Hobbs, and E. Sabatino, Proc. SPIE **8016**, 80160Q (2011).
11. R. J. Weiblen, C. Florea, A. Docherty, C. R. Menyuk, B. Shaw, J. Sanghera, L. Busse, and I. Aggarwal, "Increased laser damage threshold in As_2S_3 motheye antireflective structures," in *IEEE Photonics Conference*, Burlingame, Calif. (IEEE, 2012), paper ThP3.
12. K. Han and C.-H. Chang, Nanomaterials **4**, 87 (2014).
13. J. Yamauchi, M. Mita, S. Aoki, and H. Nakano, IEEE Photon. Technol. Lett. **8**, 239 (1996).
14. Z. Y. Yang, D. Q. Zhu, M. Zhao, and M. C. Cao, J. Opt. A **6**, 564 (2004).
15. M. G. Moharam and T. K. Gaylord, J. Opt. Soc. Am. **71**, 811 (1981).
16. L. Li, J. Opt. Soc. Am. A **14**, 2758 (1997).
17. C. Florea, L. Busse, S. Bayyab, B. Shaw, I. Aggarwal, and J. Sanghera, "Anti-reflective surface structures in spinel ceramic windows," in *the 10th Pacific Rim Conference on Ceramic and Glass Technology*, San Diego, Calif. (2013), pp. S10–014.
18. D. S. Hobbs, B. D. MacLeod, E. Sabatino III, T. M. Hartnett, and R. L. Gentilman, Proc. SPIE **8016**, 80160T (2011).
19. D. S. Hobbs, Proc. SPIE **7842**, 78421Z (2010).
20. L. Busse, C. Florea, B. Shaw, S. Bayya, G. Villalobos, I. Aggarwal, and J. Sanghera, "Anti-reflective surface structures for high energy laser applications," in *Annual Directed Energy Symposium*, Santa Fe, N. Mex. (2013), paper 13-Symp-053.
21. R. J. Weiblen, C. Florea, L. Busse, B. Shaw, C. R. Menyuk, I. Aggarwal, and J. Sanghera, *Conference on Lasers and Electro-Optics (CLEO)* (Optical Society of America, 2014), paper JTh3J.4.
22. J. F. DeFord and M. R. Kozlowski, Proc. SPIE **1848**, 455 (1993).
23. X. Cheng, T. Ding, B. Ma, H. Jiao, J. Zhang, Z. Shen, and Z. Wang, *Conference on Lasers and Electro-Optics (CLEO)* (Optical Society of America, 2014), paper JTh3J.1.
24. R. M. Wood, *Laser-Induced Damage of Optical Materials* (Institute of Physics, 2003).
25. X. Jing, J. Shao, J. Zhang, Y. Jin, H. He, and Z. Fan, Opt. Express **17**, 24137 (2009).
26. D. H. Raguin and G. M. Morris, Appl. Opt. **32**, 1154 (1993).
27. M. Steel, T. White, C. M. de Sterke, R. McPhedran, and L. Botten, Opt. Lett. **26**, 488 (2001).
28. W. H. Southwell, J. Opt. Soc. Am. A **8**, 549 (1991).
29. V. R. Almeida, Q. Xu, C. A. Barrios, and M. Lipson, Opt. Lett. **29**, 1209 (2004).